Downstream porosity for the reduction of turbulence-aerofoil interaction noise

Sergi Palleja-Cabre, Paruchuri Chaitanya, Phillip Joseph, Jae Wook Kim, Matthew J. Priddin, Lorna J. Ayton, Thomas F. Geyer, Tze Pei Chong

PII: S0022-460X(22)00507-7
DOI: https://doi.org/10.1016/j.jsv.2022.117324
Reference: YJSVI 117324

To appear in: *Journal of Sound and Vibration*

Received date : 16 February 2022
Revised date : 16 September 2022
Accepted date : 23 September 2022

Please cite this article as: S. Palleja-Cabre, P. Chaitanya, P. Joseph et al., Downstream porosity for the reduction of turbulence-aerofoil interaction noise, *Journal of Sound and Vibration* (2022), doi: https://doi.org/10.1016/j.jsv.2022.117324.

Highlights

- Downstream porosity shows similar behaviour to two flat plates in a tandem configuration.
- Up to 2.8 dB reductions in overall noise are observed on realistic aerofoil geometries.
- Edge-to-edge interference is present with 180deg phase inversion between the edges.
- The noise reduction spectra are closely related to that of an effective shorter chord.

Downstream Porosity for the Reduction of Turbulence-Aerofoil Interaction Noise

Sergi Palleja-Cabre, Paruchuri Chaitanya, Phillip Joseph, Jae Wook Kim

Institute of Sound and Vibration Research, University of Southampton, Highfield, SO17 1BJ, United Kingdom

Matthew J. Priddin, Lorna J. Ayton

University of Cambridge, Cambridge, England CB3 0WA, United Kingdom

Thomas F. Geyer

Brandenburg University of Technology Cottbus, 03046 Cottbus, Germany

Tze Pei Chong

Department of Mechanical and Aerospace Engineering, Brunel University London, Uxbridge, UB8 3P, United Kingdom

---

Abstract

This paper is a predominantly experimental study into the use of porosity located downstream of an aerofoil leading edge for the reduction of turbulence interaction noise. Locating the porosity downstream of the leading edge has been shown to be beneficial in reducing the aerodynamic performance penalty compared with locating it directly at the leading edge [1], where most of the lift is generated. Noise measurements on a flat plate with downstream porosity are compared against the case of two flat plates in a tandem configuration. In both cases, the noise reduction spectra exhibit peaks of strong noise reduction at non-dimensional frequencies of $fl_d/U_c = n$, where l_d is the distance between the leading edge and the downstream edge, U_c is the convection velocity and n is an integer. To explain this behaviour requires a mechanism to be present in which a phase shift of 180° is introduced in the interaction process. In the paper we argue that the origin of this phase shift is due to secondary vorticity generated at the leading edge. Another key finding of this paper is that overall noise reductions are due to an effective shortening of the chord in which most of the radiation is produced by the section of the flat plate upstream of the porous section, leading to generally weaker radiation. Neither of these mechanisms have been reported previously in the literature. The paper concludes with noise measurements on a thin aerofoil with downstream porosity included, in which overall noise reductions of up to 2.8dB are achieved.

Keywords: Turbulence-aerofoil interaction noise, Downstream porosity, Aerofoil noise reduction, Beamforming

---

1. Introduction

Broadband turbulence interaction noise is one of the dominant noise sources in a number of aerospace applications such as modern turbofan engines. Here, broadband noise is generated through the interaction between incoming turbulent flow and downstream blades, such as Outlet Guide Vanes (OGV). Two technologies proven to be effective in reducing broadband interaction noise are leading edge serrations (undulations) [2–9] and, more recently, porosity [4, 10–16] introduced onto the OGV leading edge.

Geyer et al. [10] manufactured fully porous SD7003 aerofoils with commercially available porous materials, which they characterised by their airflow resistivity. The porous aerofoil was located within a turbulent flow, where it was shown that noise reductions generally increased with increasing flow resistivity (higher permeability). However, it was found that the use of porosity over the entire chord incurred significant penalties in aerodynamic performance (lift and drag). In a later paper Geyer et al.[11] investigated the use of porous leading edge (LE) inserts with inclined circular perforations limited to 5% of the chord. This design produced a smaller aerodynamic penalty at low angles of attack while achieving noise reductions of up to 8 dB at some frequencies. An increase of noise (4-5 dB) at high frequencies was also observed, which was attributed to the surface roughness due to the pores. More recently, Ocker et al. [12] investigated the use of 3D-metal-printed perforated leading edges in aerofoils and axial fans. Noise reductions of up to 10 dB were measured in specific frequency bands with an aerodynamic penalty of 30% in lift and drag.

An alternative design for porous aerofoils was proposed by Roger et al. [4] consisting of a porous NACA-0012 aerofoil comprising a composite layered structure of wire mesh and metal foam filled with steel wool. Measured noise reductions of 5 dB were achieved without attempting an optimization of the design parameters. Experimental studies with similar aerofoil designs consisting of a porous exoskeleton filled with foam or metal wool and a solid centre plate have been reported by Zamponi et al. [17] and Bampanis et al. [13], where noise reductions of 4 and 6 dB were measured respectively. The latter design was reported to increase the drag by 15%.

A number of porous leading edge treatments with and without centre plate were studied computationally with a lattice-Boltzmann method in a rod-aerofoil configuration by Teruna et al. [18]. The study also proposed and evaluated a serrated porous leading edge to combine the benefits of porosity and serrations, which showed improved acoustic and aerodynamic performance relative to regular serrations. More recently, the concept of poro-serrations was further investigated to reduce rotor-stator interaction noise in a computational study of a full-scale aircraft model by [19]. It was found that applying the treatment in the outer span of the OGV is most beneficial and can yield up to 1.5 dB of overall power level with a performance penalty below 1.5 %.

Although it is clear that leading edge porosity is a promising technology for the reduction of turbulence interaction noise, the physical mechanisms of noise reduction are not fully understood. Suggested mechanisms [11] include hydrodynamic absorption of the impinging turbulence by the porous surface, viscous dissipation in the pores, and an increased effective aerofoil thickness due to thicker boundary layers. The first hypothesis was studied by Zamponi et al. [17] on a porous NACA-0024 aerofoil. Their measured data showed a weaker distortion of the turbulent flow in the vicinity of the leading edge stagnation region due to the surface permeability, which was linked to a reduction in radiated noise at low frequencies. The computational work by Teruna et al. [18] also indicates that leading edge porosity reduces the strength of the sources at the leading edge by allowing the incoming turbulence to permeate into the porous medium.

The noise reduction mechanisms of porous leading edges were also investigated by [16] for fully and partially porous flat plates. That is, extending over the full chord of the flat plate or over an extent l from the leading edge respectively. From here on, porosity is defined as the percentage of open area. In the case of a fully porous plate the noise reduction spectra were found to contain a number of peaks of maximum noise reduction at the non-dimensional frequencies of $fc_0/U_c = n$, where c_0 is the chord. In the case of a flat plate in which porosity of extent l is introduced from the leading, however, peaks in the spectra were observed at $fl/U_c = (n - 1/2)$. Different noise reduction mechanisms were proposed to explain these two different configurations. The first for fully porous aerofoils was attributed to a reduced radiation efficiency based on the assumption that the aerofoil response (pressure jump) across the porous section propagates at the flow convection speed U_c and not the acoustic speed, as is the case for a rigid aerofoil. The second mechanism was attributed to destructive interference between compact sources located at the leading edge and at the end of the porous section separated by l. Also, included in [16] were preliminary results for the case when the porous section was located downstream of the leading edge, thereby reducing adverse effects on aerodynamic performance. Noise reductions of up to 6dB were observed by introducing porosity 32% of the chord length downstream of the leading edge. A significant feature of the noise reduction spectra for this case was the presence of strong peaks occurring at frequencies of $fl_0/U_c = n$, where l_0 is the distance from the leading edge to the porous section. No satisfactory mechanism was provided to explain this phenomenon. The use of downstream porosity was also recently investigated by Ocker et al. [1] on 3D-metal-printed aerofoils and axial fans who showed that the aerodynamic performance penalty is progressively reduced when installing the porous region further downstream from the leading edge, i.e. increasing l_0. The use of downstream porosity was also investigated theoretically in [20]. In [20] the acoustic wave equation was solved with appropriate boundary conditions using the Wiener–Hopf method to predict the far field noise in which the problem was approximated by two flat plates separated by a known distance in a tandem configuration subject to an incoming harmonic vortical gust. The problem therefore effectively assumes 100% porosity in the section between the plates, which we shall show in Section 4 below, exhibits almost identical behaviour to the case of non-zero porosity. Their predictions were compared against our experimental results and found to give broad qualitative agreement, providing an approximate envelope for the measured noise reduction spectra. However, peaks in the noise reduction spectra were absent from their predictions suggesting that some of the key physics were absent from this purely acoustical solution.

2. Motivation and scope of the paper

This paper is a detailed experimental investigation into the use of downstream porosity for the reduction of aerofoil - turbulence interaction noise. This paper was motivated, not only by its noise reduction effectiveness and improved aerodynamic performance [1], but because it involves new physical principles not previously reported in the literature. Preliminary results relating to the use of downstream porosity were presented by the authors in the conference paper [21].

Noise reduction measurements were acquired in two different open jet wind tunnels to demonstrate the robustness and consistency of the noise reduction principles for aerofoils with downstream porosity. The sensitivity of the noise reductions to variations in porosity, length of the porous section, and its distance from the leading edge, were conducted on a flat plate. Porous flat plates have been demonstrated to be representative of the behaviour of thin aerofoils [16]. One of the key results of the current paper is that the noise reduction performance of a flat plate with downstream porosity is shown to have identical behaviour to that of two flat plates in a tandem configuration, i.e., where the porosity is effectively 100%. The measured data is compared to a simple analytical model in an attempt to understand the underlying noise reduction mechanisms. The flat plate results and predictions are later compared to data obtained for a thin aerofoil of 5% thickness typical of OGVs.

3. Experimental setup and procedure

3.1. Porous and tandem flat plates

For economy and ease of manufacture, measurements were made of the far field noise due to a flat plate with various arrangements of downstream porosities, situated within a turbulent flow. The baseline and porous flat plates had a mean chord (c_0) of 125 mm and a span of 450 mm. They were constructed by joining together two 1 mm thick metallic sheets to allow porous flat plate inserts 2 mm thick to be inserted between them. The step arising from these inserts into the two flat plates were grounded to ensure a smooth transition between the inserts and the flat plates. All corners were rounded and the trailing edges were sharpened to eliminate vortex shedding noise. The slotted flat plate is sketched in Fig. 1. Further details of a similar flat plate construction can be found in [22]. A parametric study was performed at the ISVR with one or more rows of circular holes downstream of the leading edge. The parameters investigated were the hole diameter (D), the spacing between holes (T), the distance from the leading edge to the (first) row of holes (l_0), and the length of the porous section (l). A diagram of the porous flat plate is depicted in Fig. 2a, where s is the span and c_0 is the total chord of the assembled slotted flat plate with the porous insert. Note that the diagram is not to scale and it represents a top view of Fig. 1. Cases with rectangular slots instead of circular holes were also tested but not included here since they provided almost identical noise reductions to the circular holes at the same porosity. Table 1 provides a summary of the flat plate configurations tested in this study, all conducted at flow speeds of 20, 40 and 60 m/s corresponding to Reynolds numbers based on chord of $Re_c = 2.4 \cdot 10^5$, $4.7 \cdot 10^5$ and $7.1 \cdot 10^5$.

Noise measurements were also made for two rigid flat plates in a tandem configuration and separated by a variable air gap to provide the limiting case of 100% porosity (see Fig. 2b).

Table 1: Summary of parametric flat plate experiments performed in the current study.

Configuration	Hole diameter, D (mm)	Spacing (T/D)	l_0 (mm)	l (mm)
Single row	1, 2, 3 and 4	1.5, 2, 2.5 and 3	l_0=5:5:45 and 55:5:65	l=D
Multiple rows (N)	1 and 2	2 and 2.5	l_0=25, 40 and 60	l=(N-2) · T+2D

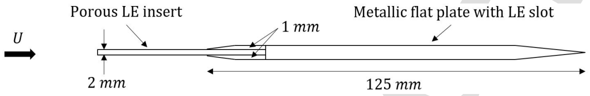

Figure 1: A sketch of the slotted flat plate use for the current experiments.

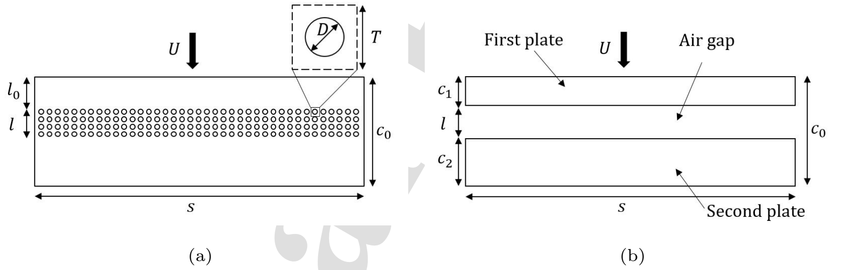

(a) (b)

Figure 2: Diagram of (a) a flat plate with downstream porosity and nomenclature and (b) of two flat plates in tandem configuration with analogous nomenclature.

3.2. Porous aerofoils

In addition to the flat plate study, the effectiveness of downstream porosity was also investigated on a NACA4505 aerofoil of 150 mm chord to verify whether the findings obtained from flat plates also apply to more realistic aerofoil geometries, such as OGVs. The aerofoil was 3-D printed with 29 rows of vertically orientated circular holes uniformly distributed between the leading and trailing edges. A hole diameter of D=3 mm and spacing of T/D = 1.67 were used in this instance. Various combinations of downstream porosity were investigated by partially covering the holes not required with a smooth thin adhesive tape. A summary of the test cases is provided in Table 2.

Table 2: Summary of parametric aerofoil experiments performed in the current study.

Configuration	l_0/c_0	l/c_0
NACA4505	0.08, 0.15, 0.25 and 0.38	0.07, 0.1, 0.13 and 0.17

3.3. ISVR open-jet test facility; far-field measurements

Far-field noise measurements were carried out at the Institute of Sound and Vibration Research's (ISVR) open-jet wind tunnel facility. The wind tunnel is located within the anechoic chamber of dimension 8 m x 8 m x 8 m as shown in Fig. 4a. The walls are acoustically treated with glass wool wedges whose cut-off frequency is 80 Hz. The nozzle has dimensions of 150 mm x 450 mm and a contraction ratio of 25:1 that provides a maximum flow speed of 100 m/s. A detailed description of the wind tunnel, including its characteristics, is presented by [23]. Side plates are mounted to the nozzle exit to support the flat plate and maintain a two-dimensional flow around it. The leading edge of the flat plate is located 150 mm (≈ one chord) downstream of the nozzle exit.

The inflow turbulence was generated by using a bi-planar rectangular grid [24] of 630 x 690 mm^2 made of wooden bars of 12 mm width separated by 34 mm. The grid was located in the contraction section 75 cm upstream of the nozzle exit. Comparison of the velocity spectra measured at 145 mm from the nozzle exit and the theoretical Liepmann velocity spectrum showed 2.5% turbulence intensity and a 7.5 mm streamwise integral length-scale were demonstrated to be in close agreement in [8]. In the absence of the turbulence grid, the nozzle delivers a clean inflow with a turbulence intensity of less than 0.5% [25].

Far-field noise measurements were made using 16, half-inch condenser microphones (B&K type 4189) located at a constant radial distance of 1.2 m from the mid span of the flat plate leading edge. These microphones are placed at emission angles of between 30° and 130° measured relative to the downstream jet axis. Measurements were carried out for 10 s duration at a sampling frequency of 20 kHz, and the noise spectra were calculated with a window size of 1024 data points corresponding to a frequency resolution of 19.53 Hz and a Bandwidth-Time (BT) product of about 200. Noise reductions are presented in terms of the Sound Power Level spectra PWL(f) calculated by integrating the pressure spectra over the polar array of microphones using the procedure described in [22]. The data used all along the manuscript was obtained in the ISVR open-jet test facility except for the source localisation results of Section 6, which were obtained at the BTU Cottbus open-jet test facility described below.

3.4. BTU Cottbus open-jet test facility; beamforming measurements

In addition to the far-field noise measurements performed in the ISVR wind tunnel facility, further measurements for a subset of cases were performed in the small aeroacoustic open jet wind tunnel at the Brandenburg University of Technology in Cottbus, Germany. These measurements at Cottbus were performed in order to verify the consistency of the measurements in a different facility and also to exploit their microphone array technology and advanced beamforming methods to identify the dominant sources on the aerofoil.

The wind tunnel is driven by a radial fan with a shaft power of 18.5 kW and can be equipped with different nozzles. For the current measurements, a circular nozzle with an exit diameter of 0.2 m was used, which allows for maximum flow velocities of up to 90 m/s with a very low turbulence intensity in the core jet (below 0.1 % at a flow speed of 50 m/s) [26]. For the current investigation of turbulence interaction noise, a turbulence grid comprising a bar width of 5 mm and a mesh width of 15 mm was mounted to the nozzle exit. At a flow speed of about 40 m/s, this grid generates turbulence with an intensity of 5.3 % and a streamwise integral length scale of 6.1 mm (see, for example, [12]).

The measurements were conducted using a planar microphone array consisting of 56 1/4th inch electret microphone capsules flush-mounted into an aluminium plate with dimensions of 1.5 m × 1.5 m. The array was located approximately 0.71 m above the flat plate and outside the flow. Figure 3 shows a schematic of the setup, including the locations of the array microphones. The data were recorded at a sampling frequency of 51.2 kHz and a duration of 40 s. Beamforming algorithms were then applied to the data using the Acoular open-source software package [27].

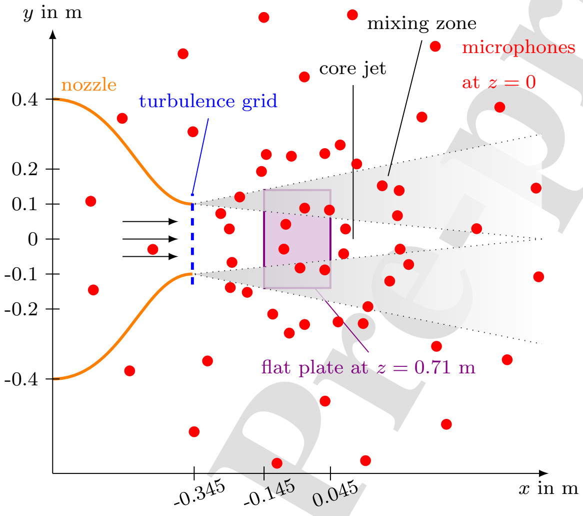

Figure 3: Schematic of the experimental setup at BTU

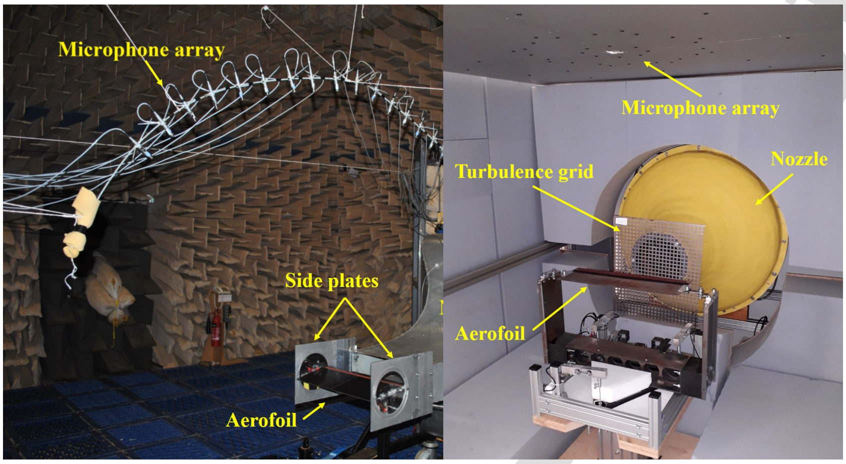

(a) (b)

Figure 4: Photograph of (a) the jet nozzle and test setup inside the ISVR anechoic chamber and (b) the BTU Cottbus open-jet test facility.

4. Acoustic performance of downstream porosity and comparison with tandem flat plates

We first provide an overview of the noise reduction spectra due to the introduction of downstream porosity on flat plates and demonstrate its equivalence to two tandem flat plates. The latter may be considered to be the limiting case of a fully porous (pressure release) downstream section.

The sound power level noise spectra due to a flat plate with downstream porosity of $D = 3$ mm and $T = 5$ mm were measured and compared against that relative to a rigid plate of chord c_0. The noise reduction spectra are presented in Fig. 5a. Also shown in Fig. 5b are the results for the two tandem flat plates. In both figures, results are presented for various values of l_0 at a constant length of the porous section $l(= l_d - l_0)$. In both the porous (Fig. 5a) and tandem (Fig. 5b) configurations, peaks in the noise reduction spectra are well defined and closely occur at the non-dimensional frequencies of fl_d/U_c, where l_d is the distance between the two leading edge discontinuities and U_c is the convection velocity ($U_c \approx 0.7U$ [28]). We note that very similar results are also obtained at other inflow velocities U.

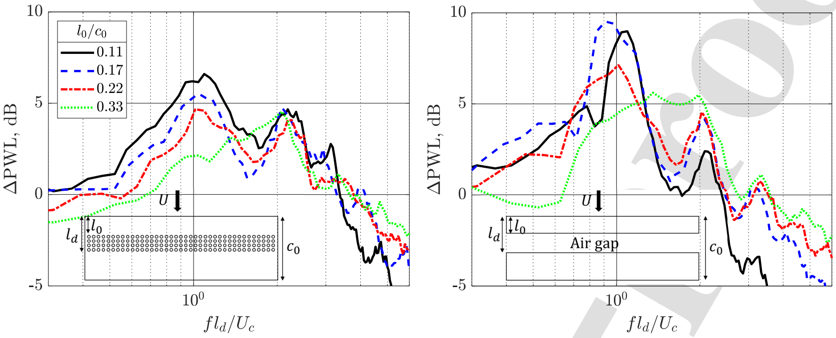

(a) (b)

Figure 5: Sound power noise reduction spectra for $l/c_0 = 0.12$, 40 m/s and various values of l_0 for (a) porous flat plates with D=3 mm and T/D=2.5 mm, and (b) tandem configurations.

The results in the Fig. 5 reveal that noise reductions due to the flat plate with downstream porosity and with air gap must have similar mechanisms by virtue of their similar spectra and peaks occurring at the same non-dimensional frequencies. The noise reduction spectra in both cases comprises a number of peaks superimposed on a broad spectrum that decays with increasing frequency, with the air gap providing higher levels of noise reduction than when porosity is introduced. The unexpected aspect of these results is that noise reduction peaks are observed at $fl_d/U_c = n$, which would ordinarily imply that, at these frequencies, the leading edges radiate in-phase and noise reductions are weakest. However, the precise opposite behaviour is observed, and the two edges must radiate in anti-phase to produce these peaks in the noise reduction spectra. We hypothesise that an additional mechanism should therefore exist by which an additional π phase change occurs to produce the strong levels of destructive interference at these frequencies. This mechanism has not been previously reported and is explored below in Section 7.

5. Sensitivity studies on flat plates with downstream porosity

5.1. Sensitivity of noise reductions to the downstream location

Figure 5 demonstrates that introducing porosity downstream of a leading edge has the potential to provide significant levels of noise reduction without directly modifying the leading edge where most of the lift is generated. For simplicity, we first investigate the noise reductions due to a single row of holes and its dependence on the downstream distance l_0 from the leading edge. The downstream distance was varied between $l_0/c_0 = [0.05-0.35]$ with D=1 mm and T/D=2.5 (13% porosity). Note that the measurements were repeated for D=2, 3 and 4 mm where almost identical noise reductions at the peak frequencies were obtained but with much higher levels of self-noise as D is increased. All subsequent measurements were therefore made at the smallest diameter D=1mm. The PWL spectra for three values of l_0/c_0 are shown in Fig. 6 in the presence of grid-generated turbulence, labelled in the figure as Turbulence Interaction Noise (TIN). Also shown are the Self Noise spectra, labelled SN, produced in the absence of the grid to allow the relative contributions between interaction noise and self-noise to be determined. Note that the term Self Noise is used to refer to all noise sources present with clean inflow, such as trailing edge noise and roughness noise.

Peak noise reductions in total noise can be clearly observed in Fig. 6 (thin solid curves) at the frequencies close to $fl_0/U_c = n$, as reported in [16], which are characterised by 'deeps' in the spectrum at those frequencies. Noise reductions become progressively weaker as the row of holes is located further downstream of the leading edge from Fig. 6a to Fig. 6c. However, the reductions in total noise between the porous case (thin solid curve) and the baseline (thick solid curve) are limited over some frequencies by additional self-noise induced by the porous section (dashed curve), which is discussed next.

A distinct feature in the self-noise spectra of porous plates in Fig. 6 (dashed curve) is that it exhibits a number of peaks also at the frequencies close to $fl_0/U_c = n$, at which maximum noise reductions in total noise (thin solid curve) have been observed. This phenomenon is particularly pronounced when the row of holes is located closest to the leading edge (Fig. 6a) and negligible when is located well downstream (Fig. 6c), and it is therefore likely to be related to the higher levels of unsteady lift in this region, although more detailed analysis is required to confirm this hypothesis.

When the holes are introduced close to the leading edge, reductions in interaction noise are greatest, as is the increase in self noise, as shown in Fig. 6a. At the furthest distance from the leading edge, the reductions in interaction noise, and increases in self noise, are the smallest (Fig. 6c). A balance between these two sources is therefore achieved at intermediate distances around $l_0/c_0 = 0.26$ where the greatest overall noise reductions are observed.

The existence of a range of distances l_0/c_0 which provide roughly the same overall noise reduction for a balance between addition self-noise at small values of l_0/c_0 and weak reductions in interaction noise that occurs at large values of l_0/c_0 is shown explicitly in Fig. 7, in which the overall noise reductions, ΔOPWL, are plotted against l_0/c_0 over the range of $l_0/c_0 = [0.2 - 0.3]$ at the two flow speeds of 40m/s and 60m/s. At a distance of $l_0/c_0 = 0.26$ reductions in overall noise of 0.75 dB are achieved. However, reference to Fig. 6 indicates that noise reductions of up to 6 dB may be achieved at the first peak frequency $fl_0/U_c = 1$.

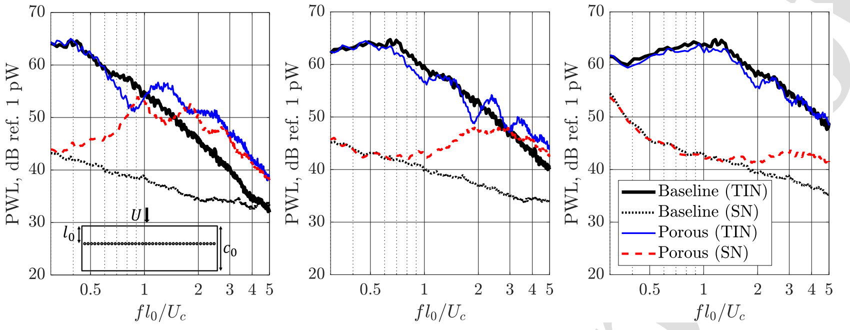

(a)

(b)

(c)

Figure 6: Sound power noise spectra for a single row of holes for (a) $\boldsymbol{l_0/c_0 = 0.09}$, (b) $\boldsymbol{l_0/c_0 = 0.14}$, and (c) $\boldsymbol{l_0/c_0 = 0.26}$ with D=1 mm, T/D=2.5 mm and U=40 m/s.

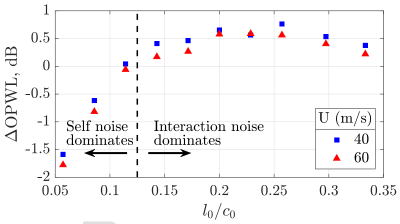

Figure 7: Overall PWL noise reduction for single row of holes and different $\boldsymbol{l_0/c_0}$.

5.2. Sensitivity of noise reductions to the chordwise-length l of the porous section

The previous section has indicated that introducing just a single row of holes well away from the leading edge is capable of delivering peak noise reductions of up to 6 dB and of 0.75 dB of OPWL. We now investigate the influence on the noise reductions to the chordwise-extent l of the porous section. In this study, the distance from the leading edge to the first row of holes is kept constant at $l_0/c_0 = 0.14$, which according to Fig. 7, is the smallest distance at which significant levels of overall noise reduction occur. The hole diameter and separation distance were kept constant such that D=1 mm and T/D=2.5. Multiple rows of holes were investigated for odd numbers between 3 and 11 corresponding to lengths of the porous section in the range of $l/c_0 = [0.02-0.13]$.

The PWL spectra for just three representative values l/c_0=0.02, 0.08 and 0.13 is shown in Fig. 8 plotted against fl_d/U_c.

The chordwise-extent of the porous section can be observed to have a pronounced effect on both the total noise radiation (thin solid curve) and the self-noise radiation (dashed curve). The most significant effect can be observed at the first peak frequency $fl_d/U_c = 1$ where total reductions increase markedly with the number of rows from 3dB for $l/c_0 = 0.02$ (Fig. 8a) to 13 dB for $l/c_0 = 0.13$ (Fig. 8c). However, self-noise also increases significantly with increasing l which therefore affects the overall noise reduction. The reduction in overall noise is plotted in Fig. 9 versus l/c_0 at the two different flow speeds.

The overall noise reductions plotted in Fig. 9 reveal a much higher dependence on the chordwise-extent of porous section l than the downstream location of the single row of holes l_0 plotted in Fig. 7. Maximum noise reductions can be observed for $l/c_0 = 0.08$ at both flow speeds, which yields reductions in overall noise OPWL of between 0.75 and 1.75 dB. Above this value of l/c_0 noise reductions fall sharply due to increased levels of self-noise, as seen in Fig. 8c. We note that the overall noise reductions are much more sensitive to l at the lower flow speed of 40m/s where the noise reductions are greatest.

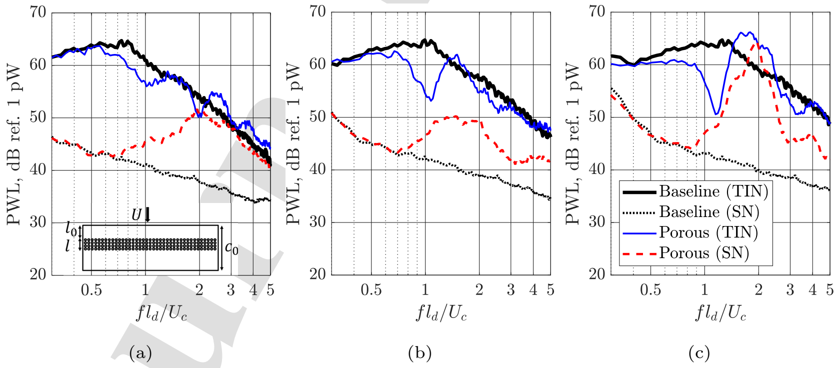

(a)

(b)

(c)

Figure 8: Sound power noise spectra for for multiple rows of holes with $l_0/c_0 = 0.14$ for (a) $\boldsymbol{l/c_0 = 0.02}$, (b) $\boldsymbol{l/c_0 = 0.08}$, and (b) $\boldsymbol{l/c_0 = 0.13}$ with D=1 mm, T/D=2.5 mm and 40 m/s.

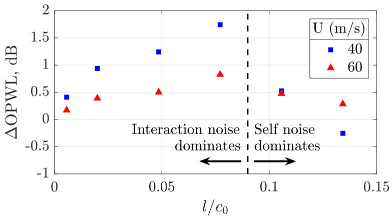

Figure 9: Overall PWL noise reduction for a fixed $l_0/c_0 = 0.14$ and different $\boldsymbol{l/c_0}$.

6. Source localisation

In this section, we investigate the source distribution over the surface of the porous flat plate obtained using the microphone array beamformer at the BTU Cottbus open-jet facility and compare it against those of the baseline plate. The porous flat plate has a downstream porosity comprising of three rows of holes of D=3 mm and T=5 mm, equivalent to $l/c_0 = 0.06$, at a downstream distance of $l_0/c_0 = 0.21$. Source maps were computed over a prescribed frequency range using the DAMAS (Deconvolution Approach for the Mapping of Acoustic Sources) beamforming algorithm [29]. This algorithm has been shown to provide superior resolution at low frequencies [30] compared to delay-and-sum beamforming. The source maps were generated in the plane of the flat plate over a square region with dimensions of 0.6 m, which extends beyond the chord and span of the flat plate.

The far-field PWL noise reduction spectra measured at the ISVR and the beamformed PWL measurements at BTU are compared in Fig. 10a to assess their consistency. In order to suppress extraneous noise sources, such as those from the shear layer and the grid, the source maps were integrated over a sector defined to include only the leading and the trailing edge regions within the core jet. Whilst there are deviations between the two spectra of up to 5dB, particularly at high frequencies, both spectra exhibit well-defined peaks at the three frequencies of approximately fl_d/U_c= 1, 2, 3. The closest agreement is obtained at the second peak frequency in the frequency range of f=[1-1.5] kHz.

Despite the differences in the two wind tunnels, and the processing methods used, similar qualitative behaviour is observed in both facilities only for frequencies below 1.5 kHz. The analysis will therefore be limited to frequencies below this threshold.

Source maps are presented in Fig. 10 at the two narrowband frequencies of f=850Hz and 1,100Hz. These frequencies correspond to the non-dimensional frequencies of fl_d/U_c=[1.5 1.9], indicated by vertical thick lines in Fig. 10a, at which the noise reduction spectra dip and peak respectively. The source maps for the baseline plate are indicated in Figs. 10b-10c, while the corresponding maps after porosity is introduced are shown in Figs. 10d-10e. Sources due to the grid and the shear layer interacting with the plate are clearly seen, which are well away from the region of integration shown by the rectangular dashed box. The source maps for the baseline plate at the two frequencies fl_d/U_c=1.5 and 1.9 shown in Figs. 10b-10c respectively, indicate the dominance of leading edge sources, which extend over most of the aerofoil down to the trailing edge, where the source levels are weaker. This behaviour is similar to the radiating chord-wise surface pressure distribution deduced by Casagrande et al [31] for leading edge noise.

The source map corresponding to $fl_d/U_c = 1.5$ following the introduction of downstream porosity is shown in Fig. 10d. Consistent with the noise reduction spectra in Fig. 10a the source maps with and without porosity are similar and indicate no significant reduction in radiated noise at this frequency. At the higher frequency $fl_d = 1.9$, however, at which the first peak in the noise reduction spectra occurs in Fig. 10a, significant reductions in source levels are observed over the entire chord. It is important to recognise that the source region just upstream of the leading edge in Fig. 10e is the result of the jet shear layer interacting with the plate. This source region appears to occur away from the shear layer but is an artefact of the relatively poor beamformer resolution at this low frequency. Source maps at the same frequency in the absence of the grid (aerofoil self-noise) show similar source maps (not shown here for brevity), thereby confirming this hypothesis.

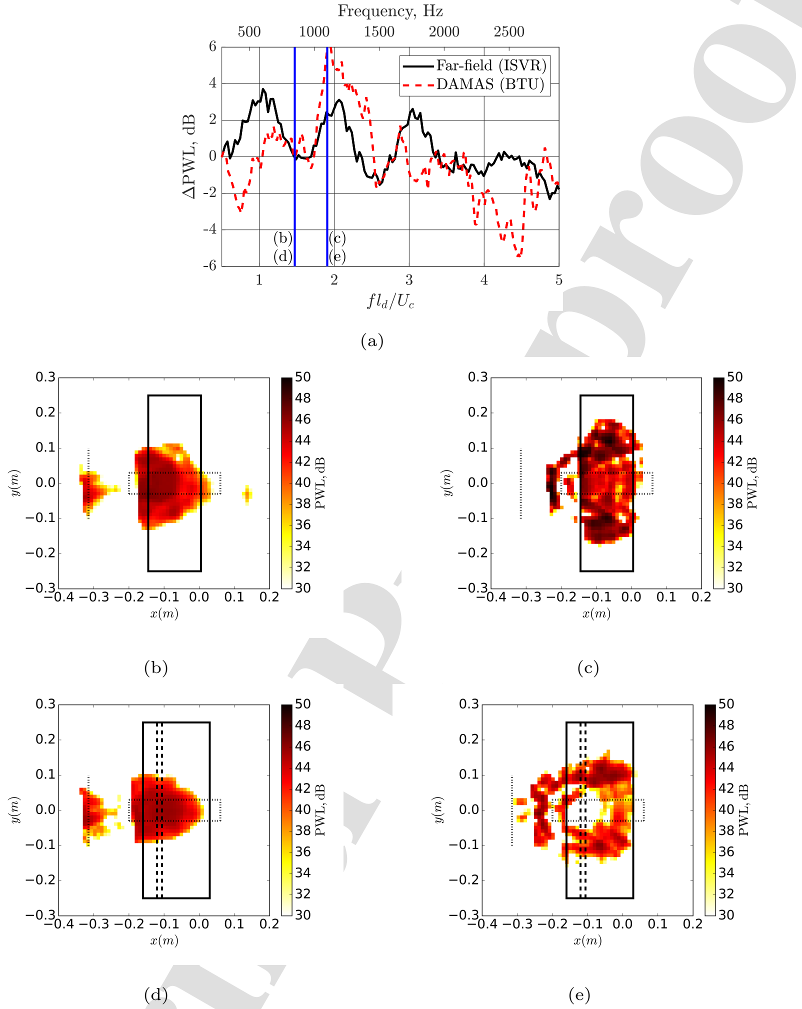

Figure 10: (a) Comparison of the far-field PWL (ISVR) and beamformed PWL using DAMAS (BTU), and beamforming sound maps for the baseline (b)-(c) and porous (d)-(e) cases. The narrowband frequencies of (b)-(d) and (e)-(g) are f=[850, 1100] Hz respectively, corresponding to fl_d/U_c=[1.5 1.9]. In the sound maps the vertical dotted line at x=-0.31 m indicates the nozzle exit, the dotted rectangle the integration sector, and the vertical dashed lines the limits of the porous section.

7. Noise reduction mechanism and analytical model for aerofoils with downstream porosity

The noise reduction mechanisms due to porous leading edges and fully porous plates were investigated by [16] for thin aerofoils, where two distinct mechanisms were proposed. One was interference between the two leading edges separated by l_0 due to interaction with the impinging turbulent flow. The other was due to a cut-off phenomenon in the case of fully porous aerofoils in which the pressure jump was assumed to propagate at the convection speed and not the acoustic speed, as in the case of rigid aerofoils. The two mechanisms were predicted to give peaks in the noise reduction spectra at non-dimensional frequencies of $fl_0/U_c = (2n+1)/2$ and $fc_0/U_c = n$ respectively.

Priddin et al.[20] have also explored the noise reduction mechanism of a flat plate upstream of a semi-infinite leading edge subject to a harmonic vortical gust. Predictions of the noise reduction spectra obtained analytically from solutions of the wave equation with appropriate boundary conditions imposed were found to capture the envelope of the experimental noise reduction spectra, but not the distinctive peaks and dips. The predicted noise reduction spectra due to Priddin were found in [21] to be consistent with an effectively shorter chord equal to the chord of the upstream plate. The radiation due to the downstream leading edge was therefore found to be relatively weak. We note that in this essentially inviscid solution the effects of secondary vorticity are precluded.

However, the mechanisms proposed in [16, 20, 21] individually cannot explain the shape of the noise reduction spectra, which comprises a number of distinct peaks at $fl_d/U_c = n$, superimposed on a broad ‘envelope’ that decays with increasing frequency. The peaks are particularly pronounced in the case of the tandem flat plates in Fig. 5b where noise reductions of up to 10dB are observed. In this case, the air gap cannot support a pressure jump and hence the cut-off mechanism cannot exist. Therefore, a possible mechanism that can explain the peaks at $fl_d/U_c = n$ is the presence of highly coherent interference between the radiation from the two leading edges. However, to explain destructive interference at the frequencies of $fl_d/U_c = n$, where the two leading edges would usually be expected to radiate in-phase, an additional phase shift of 180° must also be present. We now propose a new mechanism in order to explain the cause of this additional phase inversion that does not appear to have been recognised in the literature.

We hypothesise that the additional phase shift necessary to explain the noise reduction peaks at $fl_d/U_c = n$ is caused by secondary vorticity generated near the first leading edge interacting with edges further downstream. The phase inversion arises because its sense of rotation is opposite to that of the initial vortex. The existence and significance of secondary vorticity in aerofoil noise generation were first recognised by [32] in a fundamental numerical study of leading edge noise due to flat plates. In [32] it was shown that secondary vorticity is induced as a result of nonlinear interactions between the aerofoil and the impinging vortex. This secondary vortex then convects towards the trailing edge and was a significant source of trailing edge noise.

Recent, detailed analysis has suggested that all noise reduction mechanisms proposed in [16, 20, 21] must be simultaneously present to explain the characteristics of the noise reduction spectra described above. In this section, we further develop the simple analytic model proposed in [16] that combines all aforementioned noise reduction mechanisms, namely (i) edge-to-edge interference, (ii) phase inversion due to secondary vorticity, (iii) cut-off effects across the porous section and (iv) reduced effective chord. Predictions from the model will be compared against experimental data.

Consider a flat plate aligned with the mean flow along the y_1 direction, as sketched in Fig. 11. The figure shows three distinct sections. The first section is rigid and extends from the leading edge at $y_1 = 0$ to the start of the porous section at $y_1 = l_0$. The second is a porous section of length l that extends between $l_0 < y_1 < l_d$. The third section is a rigid flat plate with leading edge at $y_1 = l_d$ and extends to infinity in the streamwise direction since the trailing edge is not believed to contribute significantly to the noise reduction mechanism.

We now elucidate the main assumptions of the simple analytic model based on the proposed noise reduction mechanisms, whose main components are listed below and sketched in Fig. 11:

1. The impinging initial vortex, assumed here to rotate in the clockwise sense, approaches the first leading edge ($y_1 = 0$) at the free stream velocity U, causing a downwash velocity (Fig. 11a). The initial vortex interacts with the upstream leading edge to generate a localised compact pressure jump at $y_1 = 0$ equal to $\Delta p_0 \delta(y_1)$, where δ is the Dirac delta function, as shown in Fig. 11d. Interaction of the leading edge with the initial vortex induces a pressure jump that propagates along the plate to $y_1 = l_0$, which behaves similar to a trailing edge. Radiation from this upstream section therefore occurs with an effective chord equal to l_0, which is therefore generally weaker than the baseline airfoil of larger chord.

2. A secondary vortex is induced in response to the impinging vortex due to the non-linear mechanisms proposed in [32] (Fig. 11b). The secondary vorticity is assumed to remain unchanged as it convects downstream at the convection speed U_c. The sense of rotation of the secondary vortex will be opposite to the main vortex and will therefore introduce a phase inversion of 180° upon interaction with edge discontinuities relative to the impinging vortex (Fig. 11c). The initial vortex has now become bisected by the flat plate, as shown in Fig. 11b.

3. The secondary vortex interacts with the porous section to generate a pressure jump that propagates at the convection speed U_c across the porous section $l_0 < y_1 < l_d$, which at a single frequency is of the form $\Delta p(y_1)\mathrm{e}^{-\mathrm{i}\omega y_1/U_c}$, as indicated in Fig. 11d. Since in subsonic flows the propagation speed is lower than the speed of sound a, radiation from this section is considerably less efficient than for a rigid aerofoil, in which the Δp propagates at the supersonic speed $a + U_c$, and is therefore essentially 'cut-off'. It is well established in classical radiation theory that an essential requirement for efficient radiation is that the phase speed of a

propagating disturbance must exceed the sound speed [33]. This does not exist in the case of tandem flat plates since the air gap cannot support a pressure jump.

4. The secondary vortex reaches the end of the porous section and interacts with the edge discontinuity between the porous and rigid sections to generate a compact source at $y_1 = l_d$ of the form $\Delta p_{l_d}\delta(y_1 - l_d)\mathrm{e}^{-\mathrm{i}\omega l_d/U_c}$, where the phase shift $\omega l_d/U_c$ is included to account for the propagation delay between the two leading edges. This source is also shown in Fig. 11d. It is fundamentally important to recognise that since the bisected initial vortex has zero velocity component normal to the flat plates, no noise is radiated by the initial vortex for $y_1 \geq l_0$, which is entirely consistent with the experimental data showing strong noise reduction peaks at $fl_d/U_c = n$.

The mean square pressure $\overline{p^2}$ due to a flat plate with downstream porosity is therefore assumed to be the sum of the radiation $\overline{p^2}_{c=l_0}$ due to the upstream section with effective chord l_0 and the radiation $\overline{p^2}_{\mathrm{Int}}$ due to the interference mechanisms described above,

$$\overline{p^2}(x_1, x_2, \omega) = \overline{p^2}_{c=l_0}(x_1, x_2, \omega) + \alpha\overline{p^2}_{\mathrm{Int}}(x_1, x_2, \omega) \tag{1}$$

where α is a non-dimensional factor that controls the balance between the radiation due to the upstream section and due to interference mechanisms, which will be adjusted to give best fit to the measured data.

We first evaluate the radiation $p_{\mathrm{int}}(x_1, x_2, \omega)$ due to interaction by substituting the three source terms listed above into the chord-wise radiation integral due to Amiet [34] and integrating over the chord to give the following expression for the far-field acoustic pressure,

$$\begin{aligned} p_{\mathrm{int}}(x_1, x_2, \omega) \approx \frac{x_2}{4\pi a\sigma^2}\Bigg\{ &\int_0^{l_d} \left[\Delta p_0 \delta(y_1) + \Delta p_{l_d}\delta(y_1 - l_d)\mathrm{e}^{-\frac{\mathrm{i}\omega l_d}{U_c}}\mathrm{e}^{-\mathrm{i}\pi}\right]\mathrm{e}^{-\mathrm{i}\frac{\omega}{a\beta^2}\left(M - \frac{x_1}{\sigma}\right)y_1}\mathrm{d}y_1 + \\ &\int_{l_0}^{l_d} \left[\Delta p(y_1)\mathrm{e}^{-\frac{\mathrm{i}\omega y_1}{U_c}}\mathrm{e}^{-\mathrm{i}\pi}\right]\mathrm{e}^{-\mathrm{i}\frac{\omega}{a\beta^2}\left(M - \frac{x_1}{\sigma}\right)y_1}\mathrm{d}y_1 \Bigg\} \quad , \end{aligned} \tag{2}$$

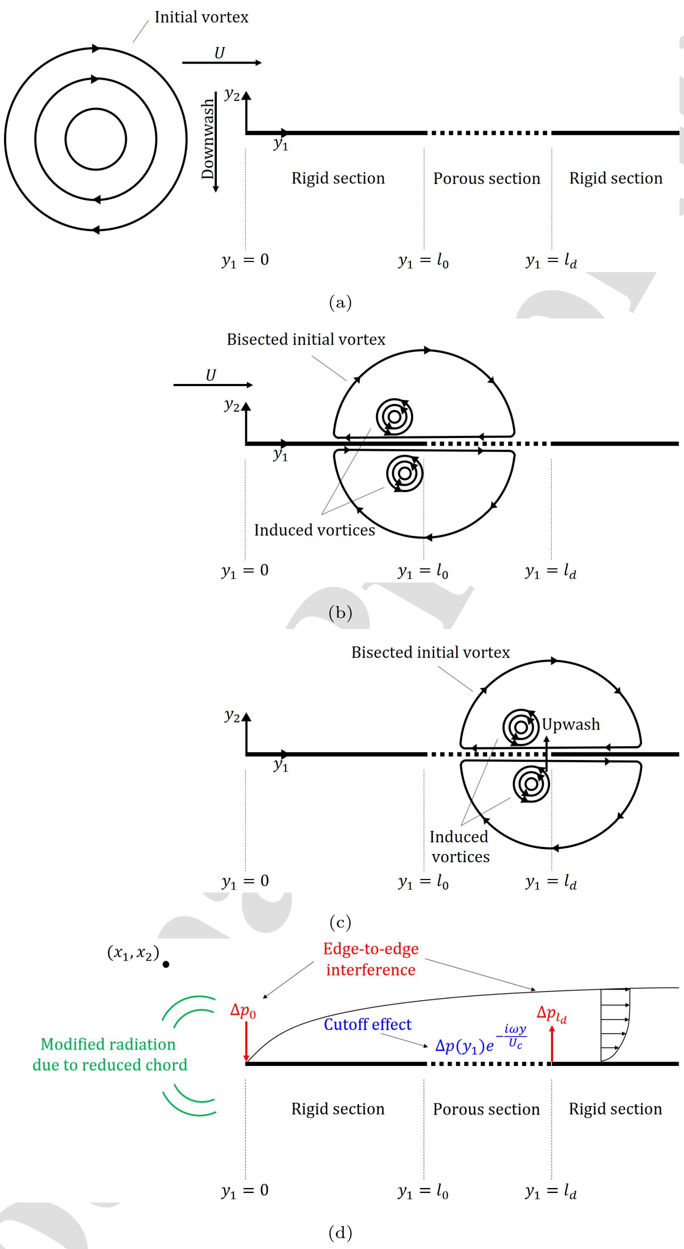

Figure 11: Schematic of the sequence of events and source regions in the proposed noise reduction mechanism; (a) Impingement of initial vortex, (b) induced secondary vorticity, (c) secondary vorticity interacting with the porous section and downstream leading edge, and (d) summary of source regions and mechanisms of noise reduction.

where (x_1, x_2) is the observer position relative to the leading edge with streamwise distance x_1, and transverse distance x_2, a is the speed of sound, $\sigma^2 = x_1^2 + \beta^2 x_2^2$, $\beta^2 = 1 - M^2$ and $M = U/a$.

In this model it is important to recognise that the interaction sources described in points (3) and (4) are in antiphase with respect to the leading edge source described in (1) due to the phase inversion of 180°, which is included explicitly by the term $\mathrm{e}^{-\mathrm{i}\pi}$.

The radiation $\overline{p^2}_{c=l_0}$ due to the upstream section, with chord l_0, is predicted using the classical theory for interaction noise due to Amiet [34] with prescribed inflow mean square velocity and turbulence integral length-scale taken from measured values.

We note that the tandem flat plate configuration is a special case of the above with $\Delta p(y_1) = 0$ in the air gap. It can be observed in Fig. 5 that when porosity is introduced the noise reduction levels at the peak frequencies $fl_d/U_c = 1, 2, 3, ...$ are generally lower than the tandem flat plate case while the dips at $fl_d/U_c = 1.5, 2.5, 3.5, ...$ are generally higher. This difference in behaviour is likely to be due to the absence of cutoff radiation across the air gap, as described in point (3) above, and a modification to the secondary vorticity by the porous section convecting towards the downstream leading edge.

7.1. *Compact porosity:* $fl/U_c < 1$

We first consider the form of the solution for the limiting case when the extent of downstream porosity is very small and hence $fl/U_c < 1$. This case corresponds to the single row of holes studied experimentally, which we assume to be located at a distance l_0 downstream of the flat plate leading edge. In this case only the compact sources at the leading edge Δp_0 and downstream edge of the holes Δp_{l_0} are considered ($l_d \approx l_0$) and hence $\Delta p(y_1) = 0$. For generality, we assume that the two compacts source strength differ by a factor K and hence $\Delta p_{l_0} = K\Delta p_0$, which upon substitution into Eq.(2) and performing the integration yields,

$$p_{\text{Int}}(x_1, x_2, \omega) \approx \frac{x_2 \Delta p_s}{8\pi a \sigma^2}\left(1 - K\mathrm{e}^{-\frac{\mathrm{i}\omega l_0}{U_c}\left[1+\frac{M}{\beta^2}\left(M-\frac{x_1}{\sigma}\right)\right]}\right) \quad . \tag{3}$$

The corresponding mean square pressure due to a single row of holes is therefore given by,

$$\overline{p^2}_{\text{Int}} \propto \left(\frac{K-1}{2}\right)^2 + K\sin^2\left(\frac{\omega l_0}{2U_c}\left[1+\frac{M}{\beta^2}\left(M-\frac{x_1}{\sigma}\right)\right]\right) \quad . \tag{4}$$

At moderate Mach numbers M maximum noise reductions are therefore predicted at the peak frequencies $fl_0/U_c \approx n$, $n = 1, 2, 3$, etc. Note that this prediction differs from that due to edge-to-edge interference presented in [16] for leading edge porosity, which predicts that $f_n l_0/U \approx n - 1/2$ where no additional phase inversion was accounted for.

7.2. Extended porosity: $fl/U_c > 1$

We now consider the more general case of a flat plate comprising an extended region of porosity $fl/U_c > 1$, represented in the experiment as multiple rows of holes. In this case, all three sources indicated in Eq. 2 will be present simultaneously and are now included in the analysis. For simplicity, we assume that the amplitude of the pressure jump over the porous section is constant. In the absence of more detailed information about the source strength distribution, we further assume that the pressure jump over the porous section per unit length is equal to that at the two leading edges Δp_0 and Δp_{l_d}. After integration, the resultant acoustic pressure is of the form,

$$p_{\text{Int}}(x_1, x_2, \omega) \approx \frac{x_2 \Delta p_s}{8\pi a \sigma^2}\left(1 - \mathrm{e}^{-\frac{\mathrm{i}\omega l_0 \tilde{M}}{U_c}}\left[\frac{2U_c}{\mathrm{i}\omega l_0 \tilde{M}} + \mathrm{e}^{-\frac{\mathrm{i}\omega l \tilde{M}}{U_c}}\left(1 - \frac{2U_c}{\mathrm{i}\omega l_0 \tilde{M}}\right)\right]\right) \quad , \tag{5}$$

where

$$\tilde{M} = 1 + \frac{M}{\beta^2}\left(M - \frac{x_1}{\sigma}\right) \quad . \tag{6}$$

The corresponding mean square pressure due to the presence of the three sources assumed in the model is of the form,

$$\overline{p^2}_{\text{Int}} \propto \sin^2\left(\frac{\omega l_d \tilde{M}}{2U_c}\right) + \text{sinc}^2\left(\frac{\omega l \tilde{M}}{2U_c}\right) + \frac{U_c}{\omega l \tilde{M}}\Bigg\{\sin\left(\frac{\omega l_0 \tilde{M}}{U_c}\right)\left[1-\cos\left(\frac{\omega l \tilde{M}}{U_c}\right)\right] + \sin\left(\frac{\omega l \tilde{M}}{U_c}\right)\left[1-\cos\left(\frac{\omega l_0 \tilde{M}}{U_c}\right)\right]\Bigg\}, \tag{7}$$

where $\text{sinc}(X) = \sin(X)/X$. The first term is identical to Eq. (4) which accounts for edge-to-edge interference with equal source strengths ($K = 1$). The second term accounts for the contribution due to radiation from the region of extended porosity, referred to in [16] as 'cut-off radiation'. The remaining four terms account for the various interactions between the three sources.

At the peak frequencies close to $fl_d/U_c = n$ the term $\overline{p^2}_{\text{Int}}$ due to edge-to-edge interference is weakest, the radiated mean square pressure is therefore largely determined by the radiation due to the upstream chord section. From Eq. 1, therefore,

$$\overline{p^2}(x_1, x_2, fl_d/U_c) \approx \overline{p^2}_{c=l_0}(x_1, x_2, fl_d/U_c) \quad , \tag{8}$$

and hence the radiation from the upstream section provides the envelope of noise reductions.

To assess the validity of the simple model we now compare in Fig. 12 predictions of the sound power against the measured noise reduction spectra for the case of multiple rows of holes and a tandem configuration. Sound power predictions are obtained by integrating Eq. 1 over the polar angles of the microphone array, with $\overline{p^2}_{\text{Int}}$ given by Eq. 7. Note that the factor α was adjusted to provide best fit to the measured sound power spectrum in each case. Also shown in Fig. 12 is the spectrum of sound power reductions due solely to the radiation from the upstream section of chord l_0, $\overline{p^2}_{c=l_0}$.

The simple model can be observed to provide acceptable *qualitative* agreement to the behaviour of the measured sound power reduction spectrum, with both the interference peaks and general spectral shape being closely predicted. The figure shows conclusively that the overall trend in the noise reduction spectra is due to an effective shortening of the chord with interference between the different sections providing oscillations in the reduction spectra around this general trend at the non-dimensional frequencies $f_n l_d/U_c \approx 1, 2, 3$, etc.

We note from Fig. 12 that the noise reduction performance at low frequencies, $f l_d/U_c < 1$, is determined by the interference sources, which are now increasingly in-phase in this low frequency limit. In this limit, the radiation from the upstream section is relatively small, tending to 14dB reduction in noise as $f l_d/U_c \to 0$.

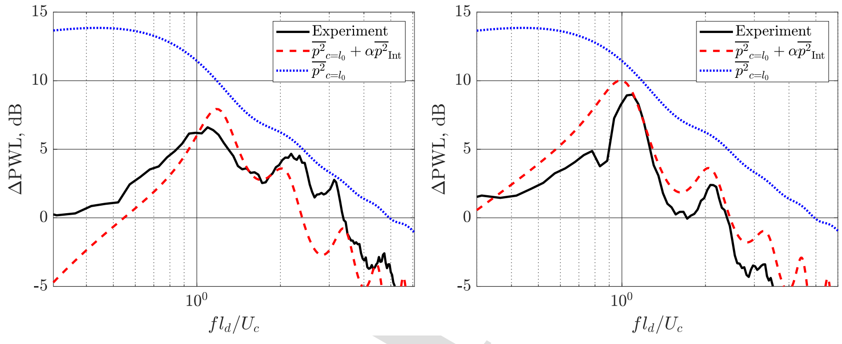

(a)

(b)

Figure 12: Comparison of the measured and predicted sound power noise reduction spectra for $l_0/c_0 = 0.11$, $l/c_0 = 0.12$ and 40 m/s for (a) a porous flat plate with D=3 mm and T/D=2.5 mm, and (b) a tandem configuration.

7.3. Discussion and limitations of the model

The analytic model for predicting the noise reduction performance of the porous flat plates based on simple source mechanisms has been shown to provide acceptable qualitative agreement with the experimental noise reduction spectra. We now interrogate the solution to identify the dominant terms and hence the principal noise reduction mechanisms.

Equation (7) for the contribution to the radiation due to interference comprises three components. The first two terms account for the radiation due to edge-to-edge interference and to 'cut-off' behaviour, respectively. The remaining terms account for the radiation due to the interaction between the different sources.

We observe from Fig. 12 that, consistent with measurement, the greatest noise reductions occur at the peak frequencies of $fl_d/U_c \approx n$, strongly implying the dominance of interference between two edges separated by l_d with an additional phase shift of 180° included.

Inspection of Eq.(7) indicates that, apart from the first term due to edge-to-edge interference, the remaining terms include factors containing the non-dimensional frequencies of $(U_c/\omega l)^2$ and $U_c/\omega l$. These terms arise from the radiation due to the porous section and are most significant at low frequencies and responsible for the weaker noise reductions in the low frequency limit. At the higher frequencies, these terms become progressively smaller with increasing non-dimensional frequency. As a consequence of the $(U_c/\omega l)$ frequency dependence, noise reductions at the first peak frequency steadily improve with increasing l, as observed in the experimental noise reduction spectra in Fig. 8.

It is noted that the intrinsic simplifying assumptions considered in the model, such as the assumption of compact sources of equal source strength, are aimed at predicting the general shape of the noise reduction spectra due to the introduction of downstream porosity. However, the model cannot predict absolute levels of noise reduction and hence the inclusion of an arbitrary factor α to control the balance of the two reduction mechanisms $\overline{p^2}_{\text{Int}}$ and $\overline{p^2}_{c=l_0}$ described above. The current model is therefore limited in this aspect and would require additional information on the spectral and spatial distribution of the pressure jump over the rigid and porous sections. The assumption of completely undisturbed convection of the secondary vorticity over the plate is also known to be a major simplification since it has been reported in [32] that the vortex energy content is transferred from larger to smaller scales as the vorticity convects over the flat plate. Improvements to the current model and testing of the underlying assumptions will be undertaken in the future by extending the computational work of [32] for cases with downstream porosity and evaluating the pressure jump over the flat plate. The current model however represents a starting point for more complex analytical studies and provides insight into the understanding of the physical noise reduction mechanisms associated with the introduction of downstream porosity on aerofoils.

8. Downstream porosity on a thin aerofoil

Having discussed the general principles of noise reduction due to the introduction of downstream porosity on flat plates we now investigate the applicability of the principle for reducing interaction noise on a thin aerofoil. The noise reduction due to the introduction of downstream porosity was measured on a NACA4505 aerofoil with a thickness - chord ratio of 5% located within grid-generated turbulent flow with 2.5% turbulence intensity at various mean flow speeds. The noise reduction spectra were measured at the two geometric angles of attack of AoA=5° and 15°, corresponding to effective angles of attack of approximately 2° and 6° once the effects of jet deflection have been taken into account [35]. The downstream location of the first row of holes was fixed at $l_0/c_0 = 0.15$ for the four different porous section lengths of l/c_0=[0.07, 0.10, 0.13 and 0.17].

The PWL noise reduction spectra for the different lengths l at the two different angles of attack are plotted against fl_d/U_c in Fig. 13. The CAD drawing for this porous aerofoil is included in the figure as an insert. As in the flat plate studies, increasing the length of the porous section can be observed to significantly enhance the noise reductions at the peak frequencies, especially at the first peak frequency $fl_d/U_c \approx 1$ and low AoA. The spectra are also found to collapse reasonably well with fl_d/U_c for the different values of l_d and flow speeds (not shown here for brevity), with distinct peaks also observed at approximately the second and third harmonic frequencies n=2 and 3.

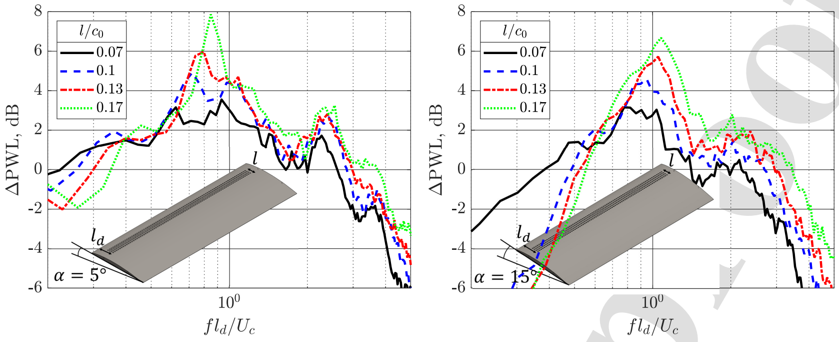

(a)

(b)

Figure 13: Sound power noise reduction spectra for a NACA4505 with $l_0/c_0 = 0.15$, D=3 mm, T/D=1.67 mm, and 40 m/s and for different lengths l of the porous section for (a) AoA=5°, and (b) AoA=15°.

An increase in noise is observed both at low frequencies ($fl_d/U_c < 0.1$) and high frequencies ($fl_d/U_c > 3$). The increase in noise at low frequencies is observed to worsen with increasing porous extent l. Moreover, the sensitivity of this increase in noise to l at low and high frequencies is amplified at the higher AoA. Measurements with a clean inflow, not included here for brevity, indicate that this increase in low frequency noise is a direct result of an increase in self-noise.

In an attempt to establish the cause of the additional noise radiation as a result of introducing downstream porosity on the aerofoil, its effect on the boundary layer development is now investigated. A hot wire was traversed vertically over a distance of 60 mm, 5 mm downstream of the trailing edge. The mean wake profiles for the baseline and porous aerofoils with $l_0/c_0 = 0.15$ and $l/c_0 = 0.10$ are shown in Fig. 14 at the highest AoA of 15° to represent the case investigated of highest additional self-noise.

The introduction of downstream porosity can be clearly seen to increase the thickness of the boundary layer on the suction side of the aerofoil. This behaviour is most likely due to flow feeding the boundary layer through the holes driven by the pressure difference across the aerofoil. Self noise therefore increases with increasing AoA as discussed earlier. We note that no discernible change in velocity profile was observed between the baseline and treated aerofoils at 0° (not shown here) and hence increases in noise at low AoA are negligible although some small increase in high frequency noise was observed due to roughness effects.

We hypothesise that larger turbulent structures created within the thicker boundary layer scattered from the trailing edge are responsible for the increase in self-noise at low frequencies. This is confirmed from measurements of the hot wire turbulence velocity frequency spectrum (not shown here). Self-noise therefore increases with increasing AoA but there remain good levels of noise reduction overall of up to 2.8dB for the cases investigated as summarised in Table 3.

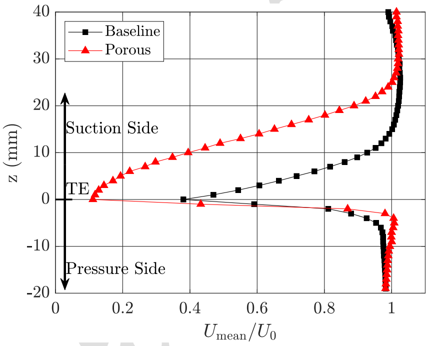

Figure 14: Comparison of the mean velocity wake profile for a baseline and porous NACA4505 with $l_0/c_0 = 0.15$, $l/c_0 = 0.10$, D=3 mm and T/D=1.67 mm at AoA=15° and 40 m/s.

Table 3: Overall PWL noise reductions (+ve) due to downstream porosity on a NACA4505 aerofoil with $l_0/c_0 = 0.15$, D=3 mm and T/D=1.67 mm for different lengths of the porous section l/c_0 and AoA at 40 m/s.

	AoA(°)			
	0	5	10	15
l/c_0	ΔOPWL (dB)			
0.07	1.7	1.2	0.7	0.1
0.10	2.3	1.5	0.4	-1.9
0.13	2.6	1.3	-0.2	-2.6
0.17	2.8	1.3	-0.2	-1.7

9. Conclusions

This paper has investigated the reductions in broadband interaction noise in flat plates and thin aerofoils by the use of porosity located downstream of the leading edge. The advantage of this approach is that the leading itself, where most of the lift is generated, is not compromised by the introduction of downstream porosity. A parametric experimental study in two different wind tunnel facilities has been conducted to assess the sensitivity of the noise reductions to the characteristic parameters of the porous section. Significant noise reductions have been obtained of up to 8dB on realistic aerofoils at some frequencies and up to 2.8dB reduction in overall noise.

A principal finding of this paper is that the noise reduction spectra for a flat plate with downstream porosity and a thin aerofoil are almost identical in shape to that of two flat plates in a tandem configuration. It has been shown experimentally that in both cases the noise reduction spectra collapse when plotted against non-dimensional frequency fl_d/U_c, where l_d is the distance between the leading edge and the downstream edge and U_c is the convection velocity. Narrowband peaks of noise reduction have been identified at frequencies

$fl_d/U_c \approx n$, where n is an integer number. These findings are explained by proposing a new noise reduction mechanism not previously discussed in the literature in which subsequent interactions downstream of the first leading edge are due to secondary vorticity driven by the initial vortex. These narrowband peaks are observed to be superimposed on a broad 'envelope', whose spectral shape has been shown to be closely related to the noise reduction due to a shorter chord equal to that of the upstream section of length l_0.

Based on these proposed mechanisms and previous analytic work on porous aerofoils, an analytical model has been proposed in an attempt to explain the general characteristics of the noise reduction spectra. The model appears to capture the general behaviour of the measured noise reduction spectra, including the peaks and the spectral envelope subject to the appropriate choice of a single empirical constant α.

Further work is required to more fully understand and establish the underpinning mechanisms of noise reduction in aerofoils with downstream porosity. Nevertheless, it is clear that this approach is potentially very useful for reducing broadband interaction noise and for achieving a good compromise between aeroacoustic benefits without significant degradation in aerodynamic performance.

Finally, we believe that downstream porosity is also beneficial in reducing tonal radiation in rotors and propellers caused by the periodic passage of mean wakes by the rotor onto the downstream stator vanes.

Acknowledgments

This work is part of the QUADPORS project funded by the EPSRC (EP/V00686X/1). P. Chaitanya would like to acknowledge the financial support of the Royal Academy of Engineering (RF\201819 \ 18 \ 194). M. J. Priddin acknowledges support from EPSRC DTP EP/N509620/1 and support from Christ's College, University of Cambridge. L. J. Ayton acknowledges support from EPSRC Early Career Fellowship EP/P015980/1. The authors would also like to thank Oscar

Propulsion for the initial funding of this project and Rolls-Royce for continued technical support.

References

[1] C. Ocker, F. Czwielong, T. F. Geyer, P. Chaitanya, M. Merkel, S. Becker, Permeable Structures for Leading Edge Noise Reduction, in: AIAA AVIATION 2021 FORUM, Virtual Event, 2021, pp. 1–20. `doi:10.2514/6.2021-2192`.

[2] A. Hersh, P. Soderman, R. Hayden, Investigation of acoustic effets of leading edge serrations on airfoils, J. Aircraft 11(4) (1974) 197–202. `doi:10.2514/3.59219`.

[3] T. F. Geyer, E. Sarradj, J. Giesler, Application of a beamforming technique to the measurement of airfoil leading edge noise, Adv. Acoust. Vib. (2012) 1–16`doi:10.1155/2012/905461`.

[4] M. Roger, C. Schram, L. De Santana, Reduction of airfoil turbulence-impingement noise by means of leading-edge serrations and/or porous materials, in: 19th AIAA/CEAS Aeroacoustics Conference, no. AIAA 2013-2108, Hilton Head, South Carolina, 2013. `doi:10.2514/6.2013-2108`.

[5] J. Kim, S. Haeri, P. Joseph, On the reduction of aerofoil-turbulence interaction noise associated with wavy leading edges, J. Fluid Mech. 792 (2016) 526–552. `doi:10.1017/jfm.2016.95`.

[6] J. M. Turner, J. W. Kim, Aeroacoustic source mechanisms of a wavy leading edge undergoing vortical disturbances, J. Fluid Mech. 811 (2017) 582–611. `doi:10.1017/jfm.2016.785`.

[7] B. Lyu, M. Azarpeyvand, S. Sinayoko, Noise prediction for serrated leading-edges, in: 22nd AIAA/CEAS Aeroacoustics Conference, no. AIAA 2016-2740, Lyon, France, 2016. `doi:10.2514/6.2016-2740`.

[8] P. Chaitanya, P. Joseph, S. Narayanan, C. Vanderwel, J. Turner, J. W. Kim, B. Ganapathisubramani, Performance and mechanism of sinusoidal leading edge serrations for the reduction of turbulence-aerofoil interaction noise, J. Fluid Mech., 818 (2017) 435–464. `doi:10.1017/jfm.2016.95`.

[9] L. Ayton, J.-W. Kim, An analytic solution for the noise generated by gust-aerofoil interaction for plates with serrated leading edges, J. Fluid Mech., 853 (2018) 515–536. `doi:10.1017/jfm.2018.620`.

[10] T. F. Geyer, E. Sarradj, J. Giesler, M. Hobracht, Experimental assessment of the noise generated at the leading edge of porous airfoils using microphone array techniques, in: 17th AIAA/CEAS Aeroacoustics Conference, no. AIAA-2011-2713, Portland, Oregon, 2011. `doi:10.2514/6.2011-2713`.

[11] T. F. Geyer, A. Lucius, M. Schrödter, M. Schneider, E. Sarradj, Reduction of turbulence interaction noise through airfoils with perforated leading edges, Acta Acust united Ac. 105 (1) (2019) 109–122. `doi:10.3813/AAA.919292`.

[12] C. Ocker, W. Pannert, M. Merkel, T. F. Geyer, F. Czwielong, F. Krömer, S. Becker, Experimental investigation of the impact of 3d-metal-printed perforated leading edges on airfoil and axial fan noise, in: AIAA Aviation 2020 Forum, Virtual Event, 2020, pp. 1–16. `doi:10.2514/6.2020-2529`.

[13] G. Bampanis, M. Roger, On the turbulence-impingement noise of a NACA-12 airfoil with porous inclusions, in: AIAA Aviation 2020 Forum, Virtual Event, 2020, pp. 1–13. `doi:10.2514/6.2020-2577`.

[14] R. Zamponi, S. Satcunanathan, S. Moreau, D. Ragni, M. Meinke, W. Schröder, C. Schram, On the role of turbulence distortion on leading-edge noise reduction by means of porosity, J. Sound Vib. 485 (2020) 115561. `doi:10.1016/j.jsv.2020.115561`.

[15] L. J. Ayton, M. J. Colbrook, T. F. Geyer, P. Chaitanya, E. Sarradj, Reduc-

ing aerofoil-turbulence interaction noise through chordwise-varying porosity, J. Fluid Mech. (2020) 1–28`doi:10.1017/jfm.2020.746`.

[16] P. Chaitanya, P. Joseph, T. Z. Chong, M. Priddin, L. Ayton, On the noise reduction mechanisms of porous aerofoil leading edges, J. Sound Vib. 485 (115574) (2020). `doi:10.1016/j.jsv.2020.115574`.

[17] R. Zamponi, D. Ragni, N. V. de Wyer, C. Schram, Experimental investigation of airfoil turbulence-impingement noise reduction using porous treatment, in: 25th AIAA/CEAS Aeroacoustics Conference, no. AIAA-2019-2649, Delft, The Netherlands, 2019. `doi:10.2514/6.2019-2649`.

[18] C. Teruna, F. Avallone, D. Casalino, D. Ragni, Numerical investigation of leading edge noise reduction on a rod-airfoil configuration using porous materials and serrations, J. Sound Vib. 494 (2021) 1–25. `doi:10.1016/j.jsv.2020.115880`.

[19] C. Teruna, L. Rego, D. Casalino, D. Ragni, F. Avallone, A Numerical Study on Aircraft Noise Mitigation Using Porous Stator Concepts, Aerospace 9 (2) (2022). `doi:10.3390/aerospace9020070`.

[20] M. J. Priddin, L. J. Ayton, S. Palleja-Cabre, P. Chaitanya, P. Joseph, Downstream Perforations for the Reduction of Turbulence-Aerofoil Interaction Noise: Part II - Theoretical Investigation, Virtual Event, 2021, pp. 1–16. `doi:10.2514/6.2021-2147`.

[21] S. Palleja-Cabre, C. C. Paruchuri, P. Joseph, M. J. Priddin, L. J. Ayton, Downstream Perforations for the Reduction of Turbulence-Aerofoil Interaction Noise: Part I - Experimental Investigation, in: AIAA AVIATION 2021 FORUM, Virtual Event, 2021, pp. 1–13. `doi:10.2514/6.2021-2149`.

[22] S. Narayanan, P. Chaitanya, S. Haeri, P. Joseph, J. W. Kim, C. Polacsek, Airfoil noise reductions through leading edge serrations, Phys. Fluids 27 (025109) (2015). `doi:10.1063/1.4907798`.

[23] T. P. Chong, P. F. Joseph, P. O. A. L. Davies, A parametric study of passive flow control for a short, high area ratio 90 deg curved diffuser, J. Fluids Eng. 130 (11) (2008). `doi:10.1115/1.2969447`.

[24] P. E. Roach, The generation of nearly isotropic turbulence by means of grids, Int. J. Heat Fluid Flow 8(2) (1987) 82–92. `doi:10.1016/0142-727X(87)90001-4`.

[25] T. P. Chong, P. F. Joseph, P. O. A. L. Davies, Design and performance of an open jet wind tunnel for aero-acoustic measurement, Appl. Acoust. 70 (4) (2009) 605–614. `doi:10.1016/j.apacoust.2008.06.011`.

[26] E. Sarradj, C. Fritzsche, T. F. Geyer, J. Giesler, Acoustic and aerodynamic design and characterization of a small-scale aeroacoustic wind tunnel, Appl. Acoust. 70 (8) (2009) 1073–1080. `doi:10.1016/j.apacoust.2009.02.009`.

[27] E. Sarradj, G. Herold, A python framework for microphone array data processing, Appl. Acoust. 116 (2017) 50–58. `doi:10.1016/j.apacoust.2016.09.015`.

[28] W. K. Blake, Chapter 2 - essentials of turbulent wall pressure fluctuations, in: W. K. Blake (Ed.), Mechanics of Flow-Induced Sound and Vibration, Volume 2, second edition Edition, Academic Press, Paris, 2017, pp. 81–177. `doi:https://doi.org/10.1016/B978-0-12-809274-3.00002-7`.

[29] T. F. Brooks, W. M. Humphreys, A deconvolution approach for the mapping of acoustic sources (damas) determined from phased microphone arrays, J. Sound Vib. 294 (2006) 856–879. `doi:10.1016/J.JSV.2005.12.046`.

[30] R. Merino-Martínez, P. Sijtsma, M. Snellen, T. Ahlefeldt, J. Antoni, C. J. Bahr, D. Blacodon, D. Ernst, A. Finez, S. Funke, T. F. Geyer, S. Haxter, G. Herold, X. Huang, W. M. Humphreys, Q. Leclère, A. Malgoezar, U. Michel, T. Padois, A. Pereira, C. Picard, E. Sarradj, H. Siller, D. G. Simons, C. Spehr, A review of acoustic imaging methods using

phased microphone arrays: Part of the "aircraft noise generation and assessment" special issue, CEAS Aeronaut. J. 10 (2019) 197–230. `doi:10.1007/s13272-019-00383-4`.

[31] F. Casagrande Hirono, P. F. Joseph, F. M. Fazi, Acoustic source distribution on aerofoils and its reconstruction from far-field array measurements, J. Sound Vib. 492 (2021) 115786. `doi:10.1016/j.jsv.2020.115786`.

[32] J. M. Turner, J. W. Kim, Trailing-edge noise generation from a flat-plate aerofoil interacting with a prescribed vortex, J. Sound Vib. 489 (2020) 115654. `doi:10.1016/j.jsv.2020.115654`.

[33] F. Fahy, P. Gardonio, Sound and Structural Vibration: Radiation, Transmission and Response, second edi Edition, Academic Press (Elsevier), London, 2007. `doi:10.1016/B978-0-12-373633-8.X5000-5`.

[34] R. K. Amiet, Acoustic radiation from an airfoil in a turbulent stream, Journal of Sound and Vibration 41 (4) (1975) 407–420. `doi:10.1016/S0022-460X(75)80105-2`.

[35] T. F. Brooks, D. S. Pope, M. A. Marcolini, Airfoil self-noise and prediction, Vol. 1218, National Aeronautics and Space Administration, Office of Management, Scientific and Technical Information Division, 1989.